



Large-scale Map of Millimeter-wavelength Hydrogen Recombination Lines around a Young Massive Star Cluster

Q. Nguyễn-Lu'ông^{1,2,13}, L. D. Anderson^{3,4,5}, F. Motte^{6,7}, Kee-Tae Kim¹, P. Schilke⁸, P. Carlhoff⁸, H. Beuther⁹, N. Schneider⁸, P. Didelon⁷, C. Kramer¹⁰, F. Louvet¹¹, T. Nony^{6,7}, S. Bühr⁹, M. Rugel⁹, J. Soler⁹, Y. Wang⁹, L. Bronfman¹¹, R. Simon⁸, K. M. Menten¹², F. Wyrowski¹², and C. M. Walmsley¹⁴

¹ Korea Astronomy and Space Science Institute, 776 Daedeok daero, Yuseong, Daejeon 34055, Korea; quangnguyenluong@kasi.re.kr

² NAOJ Chile Observatory, National Astronomical Observatory of Japan, 2-21-1 Osawa, Mitaka, Tokyo 181–8588, Japan

³ Department of Physics and Astronomy, West Virginia University, Morgantown, WV 26506, USA

⁴ Adjunct Astronomer at the National Radio Astronomy Observatory, P.O. Box 2, Green Bank, WV 24944, USA

⁵ Center for Gravitational Waves and Cosmology, West Virginia University, Chestnut Ridge Research Building, Morgantown, WV 26505, USA

⁶ University Grenoble Alpes, CNRS, Institut de Planétologie et d'Astrophysique de Grenoble, F-38000 Grenoble, France

⁷ AIM Paris-Saclay/Service d'Astrophysique, CEA/IRFU—CNRS/INSU—Univ. Paris Diderot, CEA-Saclay, F-91191 Gif-sur-Yvette Cedex, France

⁸ I. Physik. Institut, University of Cologne, D-50937 Cologne, Germany

⁹ Max Planck Institute for Astronomy, Königstuhl 17, D-69117 Heidelberg, Germany

¹⁰ Instituto Radioastrónoma Milimétrica (IRAM), Av. Divina Pastora 7, Nucleo Central, E-18012 Granada, Spain

¹¹ Departamento de Astronomía, Universidad de Chile, Santiago, Chile

¹² Max-Planck-Institut für Radioastronomie, Auf dem Hügel 69, D-53121 Bonn, Germany

Received 2017 May 21; revised 2017 June 17; accepted 2017 July 3; published 2017 August 1

Abstract

We report the first map of large-scale (10 pc in length) emission of millimeter-wavelength hydrogen recombination lines (mm-RRLs) toward the giant H II region around the W43-Main young massive star cluster (YMC). Our mm-RRL data come from the IRAM 30 m telescope and are analyzed together with radio continuum and cm-RRL data from the Karl G. Jansky Very Large Array and HCO⁺ 1–0 line emission data from the IRAM 30 m. The mm-RRLs reveal an expanding wind-blown ionized gas shell with an electron density $\sim 70\text{--}1500\text{ cm}^{-3}$ driven by the WR/OB cluster, which produces a total Ly α photon flux of $1.5 \times 10^{50}\text{ s}^{-1}$. This shell is interacting with the dense neutral molecular gas in the W43-Main dense cloud. Combining the high spectral and angular resolution mm-RRL and cm-RRL cubes, we derive the two-dimensional relative distributions of dynamical and pressure broadening of the ionized gas emission and find that the RRL line shapes are dominated by pressure broadening ($4\text{--}55\text{ km s}^{-1}$) near the YMC and by dynamical broadening ($8\text{--}36\text{ km s}^{-1}$) near the shell's edge. Ionized gas clumps hosting ultra-compact H II regions found at the edge of the shell suggest that large-scale ionized gas motion triggers the formation of new star generation near the periphery of the shell.

Key words: galaxies: star clusters: individual (W43) – galaxies: star formation – ISM: clouds – ISM: kinematics and dynamics – radio continuum: ISM – radio lines: ISM

1. Introduction

Massive stars are not formed alone but in clusters, either sequentially or simultaneously (see the review in Tan et al. 2014). Young massive star clusters (YMCs), younger than 10 Myr and more massive than $10^4 M_{\odot}$, are formed in massive turbulent molecular cloud complexes (Portegies Zwart et al. 2010; Fujii 2015). Young embedded massive proto-stellar clusters (YEMPs) are the precursors of YMCs and are deeply embedded in the dense gas at the junctions or hubs of a filamentary network where matter accretion occurs continuously (Hill et al. 2011; Schneider et al. 2012; Contreras et al. 2017; Csengeri et al. 2017). Due to the large amount of energy that massive stars inject into their local environments, they develop H II regions containing mostly ionized hydrogen gas (H II) once reaching the main sequence (e.g., Churchwell 2002).

Ionized gas can be probed using observations of radio continuum emission and recombination lines (Natta et al. 1994; Smirnov et al. 1995). For star-forming regions that suffer from high extinction, radio recombination lines (RRLs; Walmsley

et al. 1981), including those at millimeter wavelengths (mm-RRLs; Gordon & Walmsley 1990; Walmsley 1990), can be used instead of those at optical and infrared wavelengths. The mm-RRLs have two advantages over centimeter-wavelength radio recombination lines (cm-RRLs). First, they are mostly thermally broadened by microscopic gas motions and dynamically broaden by macroscopic motions and weakly broadened by pressure/impact, allowing the determination of ionized gas dynamics (Keto et al. 2008). Second, mm-RRLs are stronger than cm-RRLs, though high electron densities ($n_e \sim 10^{7-8}\text{ cm}^{-3}$) are required for their formation (Walmsley 1990; Peters et al. 2012). To date, most of the observations of mm-RRLs have used only single pointings or small interferometric maps toward strong, compact sources (Keto et al. 2008; Churchwell et al. 2010; Galván-Madrid et al. 2012; Guzmán et al. 2014; Kim et al. 2017). mm-RRLs were also detected in the 3 mm waveband surveys of the Central Molecular Zone of the Milky Way but only toward the massive Sgr B2 star-forming complex (Jones et al. 2012).

The giant H II region W43-Main is powered by the W43-YMC and lies at a trigonometric parallax distance of 5.5 kpc (Zhang et al. 2014). In the W43-YMC, more than 50 OB stars contribute to a high infrared continuum luminosity of $\sim 3.5 \times 10^6 L_{\odot}$ that adds up to $\sim 10^4 M_{\odot}$ stellar mass (Lester et al. 1985; Blum et al. 1999; Rahman et al. 2013). Radio

¹³ EACOA Fellow at KASI and NAOJ.

¹⁴ This work is dedicated to the memory of C. M. Walmsley, who made many pioneering contributions to using recombination lines as a diagnostic of the interstellar medium.

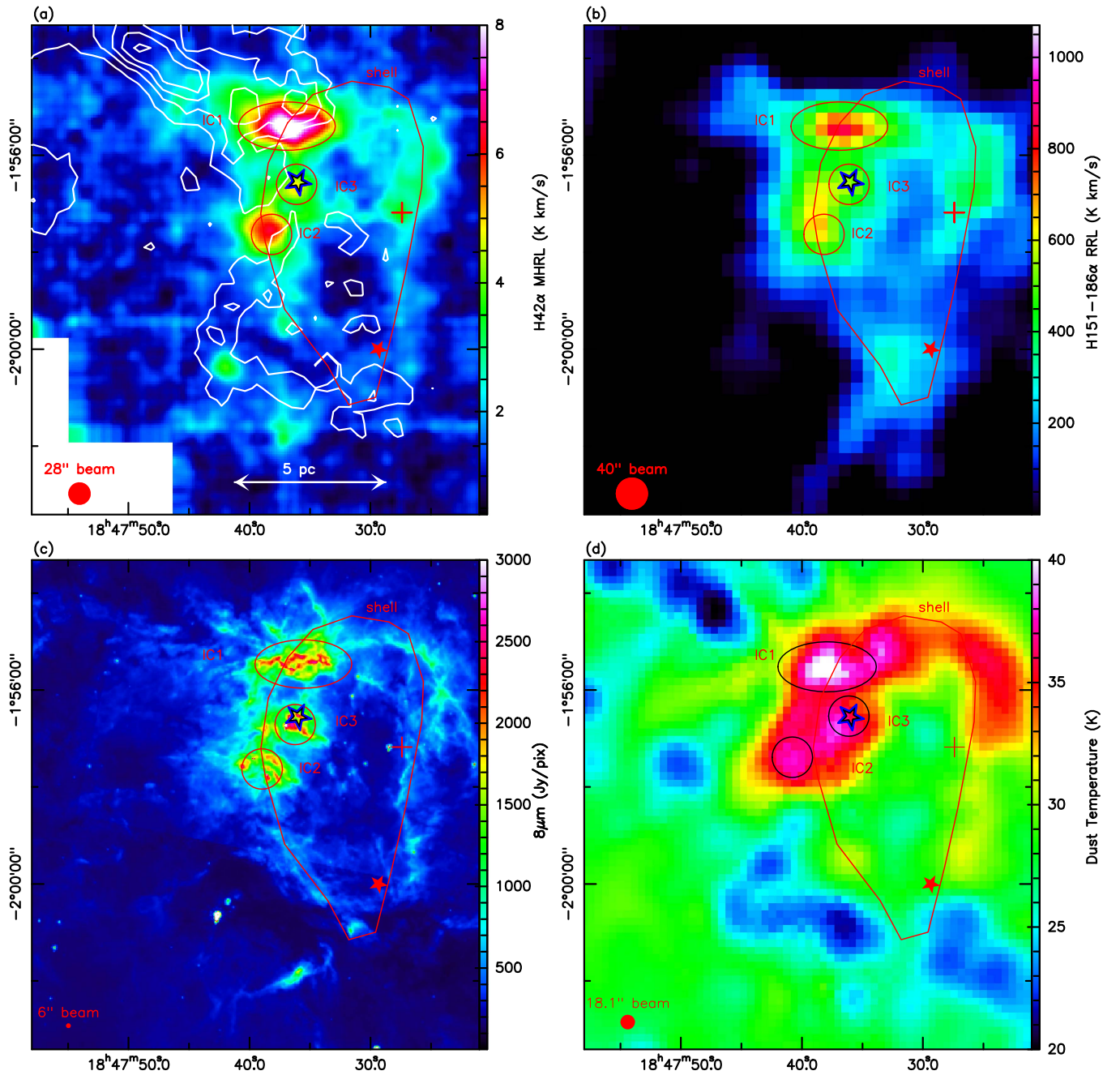


Figure 1. (a) Integrated intensity map of H42 α (color), integrated over 70–114 km s $^{-1}$, and HCO $^+$ 1–0 (contours), integrated over 80–110 km s $^{-1}$ in steps of 10, 15, 20, and 25 K km s $^{-1}$, (b) Integrated intensity map of cm-RRL integrated over 70–114 km s $^{-1}$. (c) The 8 μ m *Spitzer*/IRAC image. (d) The dust temperature map derived from *Herschel* observations (Nguyễn-Luong et al. 2013). In all panels, the red polygon denotes the position of the ionized gas shell, the red ellipses indicate the position of the ionized gas clumps, the blue star marks the position of the W43-YMC (Blum et al. 1999), the red filled star marks the position of the candidate Massive Young Stellar Object (Saral et al. 2017), and the red plus sign indicates the position where the shell’s beam-averaged spectrum in Figure 2(b) was taken.

continuum observations reveal an extended shell structure (Balsler et al. 2001), later confirmed by the H I/OH/Recombination line survey of the inner Milky Way (THOR; Bihr et al. 2015; Beuther et al. 2016). To the east of the W43-YMC, there exist the younger embedded massive proto-stellar clusters W43-MM1 and W43-MM2. They are part of the W43-Main dense cloud and are forming stars in mini-starburst mode (Motte et al. 2003; Louvet et al. 2014; Nguyễn-Luong et al. 2016). Other potential massive star formation sites such as high-mass starless clumps (Beuther et al. 2012) are also found further east, in the large-scale shell and chimney (Bally et al. 2010). The W43-Main cloud is embedded

inside the active W43 massive cloud complex (Nguyễn-Luong et al. 2011). The intense mini-starburst activity of W43 is continuously fueled by converging flows, owing to its position at the meeting point of the Scutum–Centaurus (or Scutum–Crux) Galactic arm and the bar (Nguyễn-Luong et al. 2011; Carlhoff et al. 2013; Motte et al. 2014). Similar star formation enhancement and molecular cloud interaction due to the connection of bar and spiral arms was found in the nearby galaxy NGC 3627 (Beuther et al. 2017). Recently, spatially extended low-velocity shocks traced by SiO emission, arising from cloud–cloud collisions, were discovered in the W43-MM1

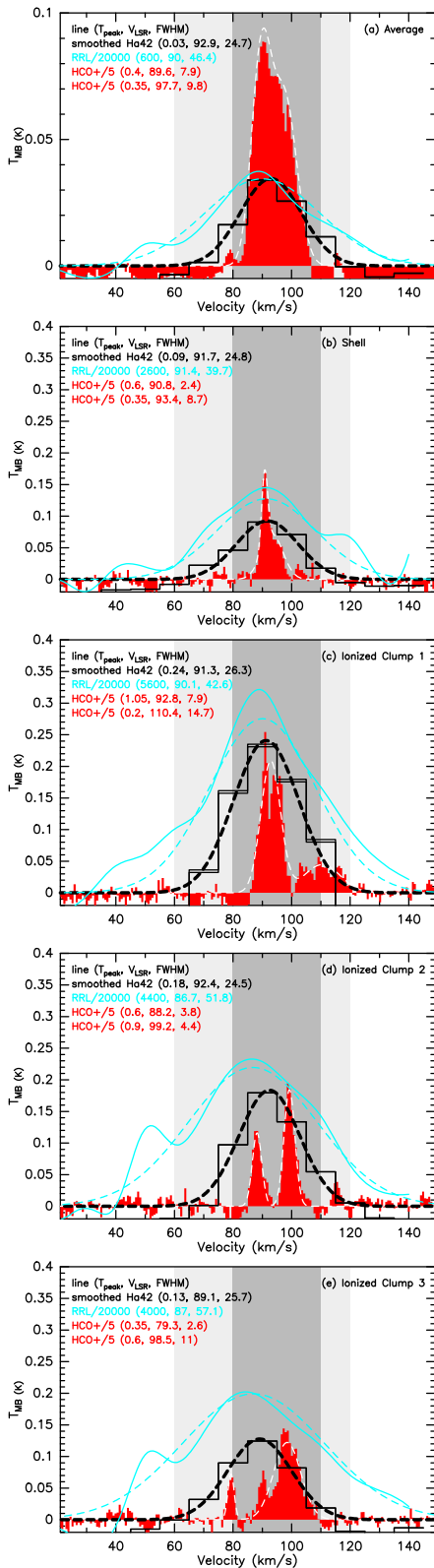


Figure 2. Spectra of H42 α smoothed to similar angular and spectral resolutions as the cm-RRLs (black), spectra of the cm-RRL (light blue), HCO⁺ 1–0 (red), and their Gaussian fits (dashed curves) (a) averaged over the entire map, (b) spectra of one beam on the western side of the ionized gas shell, (c) spectra of IC1, (d) spectra of IC2, (e) and spectra of IC3. The darker-shaded area is the main velocity range of dense gas in W43-Main and the bright shaded area is the main velocity range of the diffuse cloud traced by CO gas (Nguyễn-Luong et al. 2011). Results from Gaussian fits (T_{peak} (K), V_{LSR} (km s⁻¹), FWHM (km s⁻¹)) follow the line names shown on each plot. HCO⁺ 1–0 is fitted by a two Gaussian profile, while mm-RRL and cm-RRL are fitted by a single Gaussian profile.

and W43-MM2 ridges (Nguyễn-Luong et al. 2013; Louvet et al. 2016). These mark the boundaries between ionized and dense molecular gas and the morphologies are suggestive of an interaction between them (Motte et al. 2003).

In this Letter, we report the first large-scale high angular and spectral resolution mm-RRL map and provide the first direct dynamics evidence of the interaction between ionized and molecular gas in the region.

2. Observational Data

This Letter makes use of hydrogen recombination lines H41 α ($\nu_{\text{rest}} = 92.03443$ GHz) and H42 α ($\nu_{\text{rest}} = 85.68839$ GHz), as well as HCO⁺ 1–0 ($\nu_{\text{rest}} = 89.18853$ GHz) data cubes from the W43-HERO IRAM 30 m Large Program “Origins of molecular cloud and star formation in W43” (PIs: Frédérique Motte and Peter Schilke, Carlhoff et al. 2013; Nguyễn-Luong et al. 2013). W43-HERO conducted an 8 GHz bandwidth line mapping survey at the wavelengths of 3 mm (85–93 GHz) toward W43-Main using the Eight MIXer Receiver and the large bandwidth (8 GHz) Fast Fourier Transform Spectrometer backend at 200 kHz resolution.¹⁵ The reduced spectra are combined into gridded data cubes with a 10'' Gaussian kernel. The effective angular resolution, spectral resolution, and rms noise of these three lines are 28'', 0.67 km s⁻¹, and 17–50 mK per channel. Further information on the observations and data reduction can be found in Nguyễn-Luong et al. (2013).

Additionally, we use the radio 1.436 GHz continuum map and the stacked RRL cube from 12 hydrogen recombination lines (151 α to 186 α) out of 19 observed lines emitting in the frequency range 1.0–1.9 GHz. These data are from “The H I/OH/Recombination line survey of the inner Milky Way (THOR)” large program with the Karl G. Jansky Very Large Array introduced in Beuther et al. (2016). The final continuum data has an angular resolution of 25'' and a continuum sensitivity of 0.6 mJy/beam (0.57 K). The RRL cube is smoothed to an angular resolution of 40'' and a spectral resolution of 10 km s⁻¹, and it has an rms noise of 3 mJy/beam per 10 km s⁻¹ channel (1.1 K/10 km s⁻¹ channel). Further explanation of the observations, data reductions, and line stacking methods can be found in Beuther et al. (2016). The W43-Main ionized gas nebula is named as G30.782–0.027 in the THOR continuum source catalog (Bihr et al. 2016). We convert the flux density of the THOR data to brightness temperature using $T = 5.93 \times 10^5 \left(\frac{\theta}{\text{''}}\right)^{-2} \left(\frac{S}{\text{Jy/beam}}\right)$.

3. The Large-scale Ionized Gas Shell around the W43-YMC

Because the two mm-RRL lines in our study are at adjacent principle quantum levels, they trace the same ionized gas components. Hence, we use only the H42 α line for our analysis.

3.1. The 10 Parsec-scale mm-RRL Map

We show the first example of an extended (10 pc in length) mm-RRL map surrounding the W43-YMC in the integrated intensity map of H42 α emission in Figure 1(a). The emission is integrated from 70 to 114 km s⁻¹, which is larger than the main velocity range 80–110 km s⁻¹ of molecular gas in W43-Main (Nguyễn-Luong et al. 2011).

¹⁵ The main repository of the data is hosted by IRAM at <http://www.iram.fr/ILPA/LP004/>.

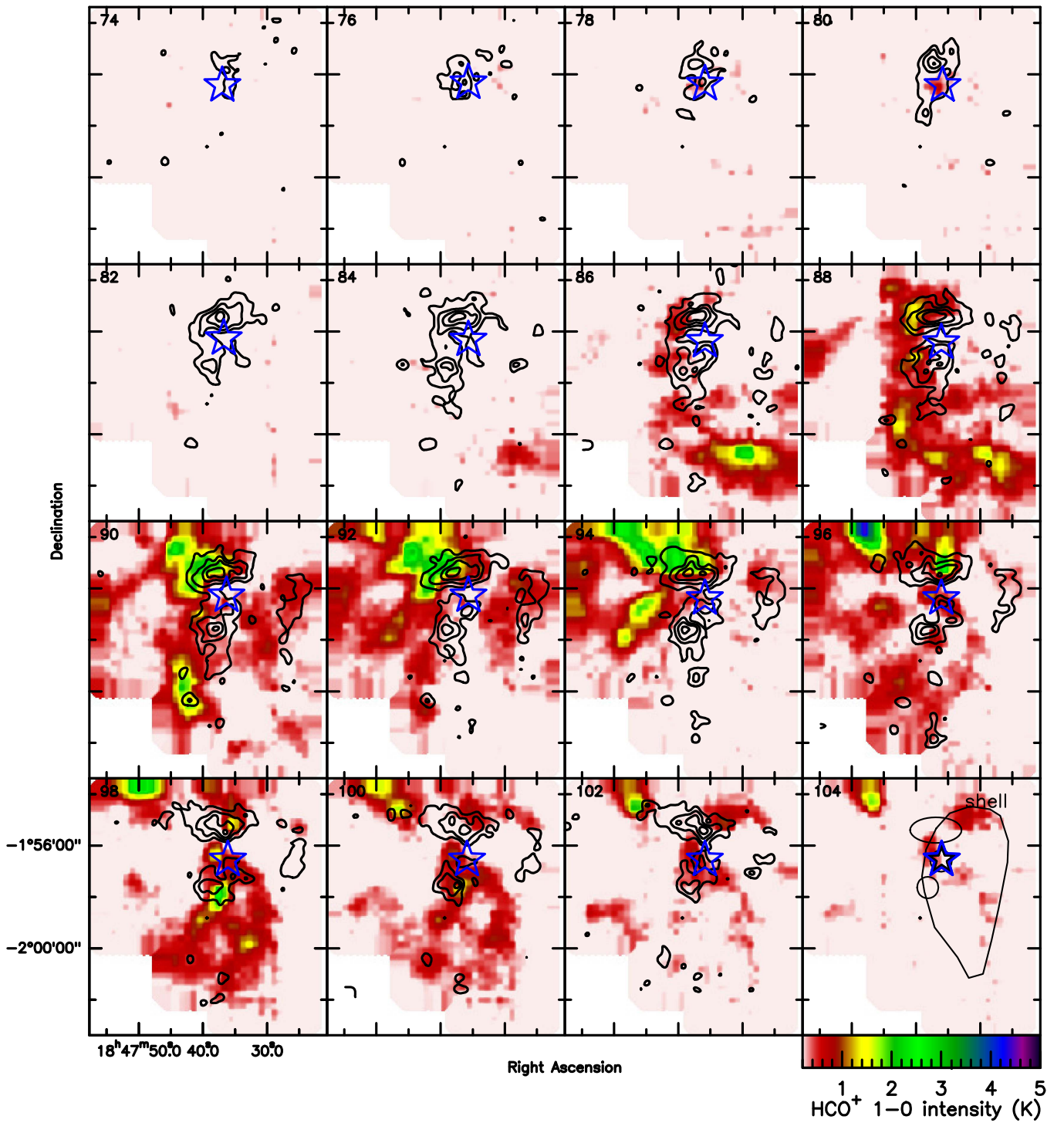


Figure 3. Channel maps between 74 and 102 km s^{-1} of $\text{H42}\alpha$ (contours in levels of 0.08, 0.14, 0.20, 0.26 K per 2 km s^{-1} channel) and HCO^+ 1–0 (colors). Both are at the native $28''$ angular resolution and in increments of 2 km s^{-1} . Symbols are denoted as in Figure 1.

The morphology of mm-RRL emission is different from that of HCO^+ 1–0. The notable feature of the integrated mm-RRL map is the oval shell with an inner cavity dominating at the western edge of the Z-shaped filaments of the W43-Main dense cloud as seen in HCO^+ 1–0 (see Figure 1(a)). The shell is well-defined in mm-RRL, cm-RRL, and $8 \mu\text{m}$ emission. In the north–south direction, the mm-RRL emission extends approximately 10 pc in projected distance, while it is about 5 pc in the east–west direction (see Figure 1). The strong

$8 \mu\text{m}$ emission shows the effect of radiation that heats the dust and PAH particles, and shocked gas. The ionizing source, W43-YMC, is located close to the eastern side of the shell where there is more dense gas and brighter RRL emission.

The cm-RRL integrated emission (Figure 1(b)) and radio continuum emission show a similar morphology surrounding the oval shape around the W43-YMC. The maximum brightness temperature of the radio continuum emission is $T_{\text{cont}} \sim 2200 \text{ K}$

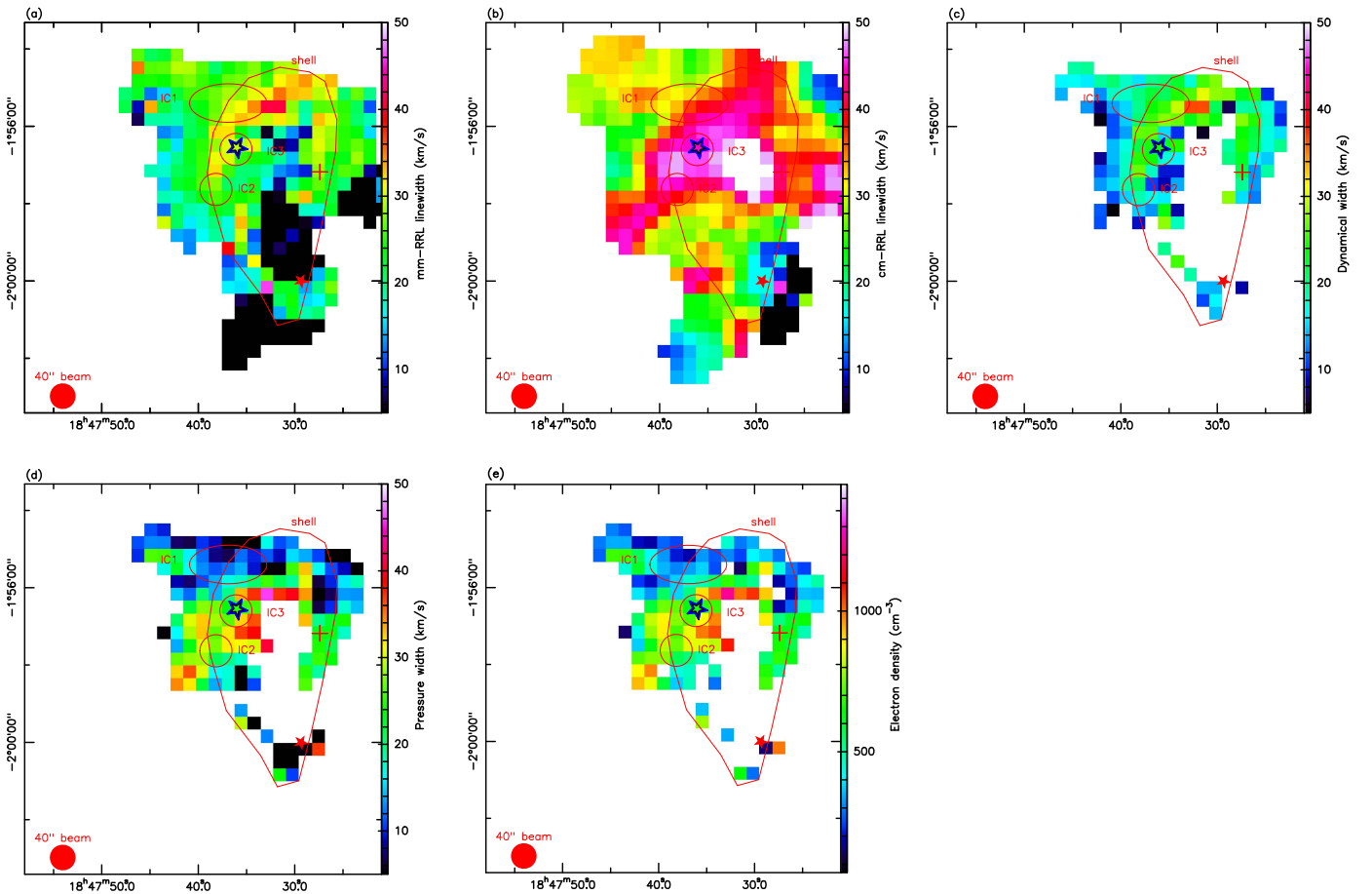


Figure 4. (a) The mm-RRL linewidth resulting from Gaussian fits. (b) The cm-RRL linewidth resulting from Gaussian fits. (c) The dynamical width resulting from Equation (4). (d) The pressure width resulting from Equation (5). (e) Electron density resulting from Equation (6). Symbols are denoted as in Figure 1.

and the ionized gas in W43-Main is dominated by free-free emission (Bühr et al. 2016). In addition to the large-scale shell, we notice that several bright ionized gas clumps (e.g., IC1, IC2, and IC3) exist at the eastern periphery of the shell, where ionized gas interacts with dense molecular gas. These ionized gas clumps coincide with the locations of several compact sources in the dust continuum map (Motte et al. 2003) and Ultra-Compact H II regions (UCH II regions, Purcell et al. 2013). The high angular resolution $8 \mu\text{m}$ map shows that the hot dust distribution resembles a spider-web filamentary structure in IC1 and curve-like structures in IC2 and IC3 (Figure 1(c)).

3.2. Expanding Ionized Gas

The high spectral resolution map of the large-scale mm-RRL emission around W43-YMC shows that the ionized gas created by the giant H II region is interacting with the dense molecular gas in the W43-Main dense cloud. In Figure 2, we plot the cm-RRL, mm-RRL, and HCO^+ beam-averaged spectra and their Gaussian fits at several locations: averaged over the whole map (a), one beam in the western side of the shell (b), one beam at the ionized clump centers (c)–(e). The interweaving of dense, neutral molecular gas traced by HCO^+ and ionized gas traced by mm-RRLs in W43-Main is visible in the similar velocity ranges of the average spectra around $80\text{--}110 \text{ km s}^{-1}$. The mm-RRL peaks are within the main velocity range $80\text{--}115 \text{ km s}^{-1}$ of W43-Main (shaded area). However, the ionized gas and neutral

molecular gas are not completely overlapping, as shown by velocity shifts in their line-of-sight velocities (see Figure 2). The HCO^+ lines show double-peak profiles in several positions where different clouds along the line of sight are interacting (Nguyễn-Luong et al. 2011) while the mm-RRL lines show only a single-peak profile. The mm-RRL width is larger than that of HCO^+ in all positions. In IC1 and IC2, the mm-RRLs have broadened blueshifted wings possibly from outflowing gas. The FWHMs of mm-RRLs are larger than pure, thermally broadened lines by $5\text{--}20 \text{ km s}^{-1}$ (see Section 4), which provides us with further evidence of outflowing ionized gas from champagne flows. The FWHMs of cm-RRLs ($\sim 28 \text{ km s}^{-1}$) are broader than those of mm-RRLs ($\sim 18 \text{ km s}^{-1}$), which shows that pressure broadening, or at least enhanced turbulence of the RRL lines, is stronger at the centimeter wavelengths (see Section 4). cm-RRLs at IC2 and IC3 have a bump at $\sim 50 \text{ km s}^{-1}$ that might come from a line-of-sight cloud.

The mm-RRL channel maps (Figure 3) show a clear positional displacement between ionized and molecular gas traced by HCO^+ . Ionized and molecular gas around W43-YMC are arranged in layers: dense ionized gas lies closest to the cluster, ionized and molecular gas co-exist in the outer shell, and dense molecular gas is distributed far from the shell. In detail, mm-RRL emission lies closer to the YMC cluster and has a sharp separation with HCO^+ , especially in the 86 and 92 km s^{-1} channels. At 94 km s^{-1} , however, ionized gas and HCO^+ merge near the location of the W43-MM1. This is also

the location where extended SiO shocks presumably from cloud–cloud collisions were discovered (Nguyễn-Luong et al. 2013). The north–south extension of the ionized gas emission is most prominent in the blueshifted part (84–95 km s^{−1}) and surrounds W43-YMC. Blueshifted emission around the 76–80 km s^{−1} channels is found in the far eastern edge and redshifted emission at channels larger than 94 km s^{−1} in the western edge of the shell revealing the extent of the expanding ionized gas. All channels show clear evidence of the ionized gas cavity where HCO⁺ is emitting around 90–92 km s^{−1}. IC2 and IC3 are strong in almost all channels from 76 to 110 km s^{−1}, thus as broad as the width of RRLs of UCH II regions (Sewilo et al. 2011) or H II regions (Anderson et al. 2015). The larger velocity range and brighter emission in the western part than in the eastern part of the channel map resemble the 2D velocity structure of the champagne flow model of the H II region; they disrupt the molecular cloud structure and create the ionized gas in the inner layer (Bodenheimer et al. 1979; Kim & Koo 2001). Alternatively, the displacement of neutral gas and ionized gas as well as the existence of ionized clumps in the shell are in agreement with the model developed by Dale & Bonnell (2011), which suggests that ionized gas only fills the pre-existing voids and bubbles, and the disruption of molecular gas by ionizing feedback is minimal. The dynamical time of the ionized gas with a velocity dispersion of 20 km s^{−1} to travel to the cloud edge at a distance of 5–10 pc from the YMC is approximately 0.2–0.5 Myr, much shorter than the age of the cluster.

4. Ionized Gas Dynamics

Aside from tracing the bulk motion of the ionized gas using their velocity information as presented in Figure 3 and Section 3.2, the mm-RRL and cm-RRL cubes are analyzed by quantifying the impact of different broadening mechanisms on the observed line widths. We determine the contribution of different broadening mechanisms to the measured linewidth using the procedure outlined by Galván-Madrid et al. (2012) or Keto et al. (2008). First, we calculate the FWHM maps pixel-by-pixel by fitting Gaussians to the mm-RRL and cm-RRL cubes. For this analysis, we smooth the mm-RRL cube to the 40'' angular resolution and 10 km s^{−1} spectral resolution of the cm-RRL cube, and regrid both mm-RRL and cm-RRL cubes to 20'' pixel. We fit only the pixels that have an integrated intensity larger than 5σ, i.e., 1.3 K km s^{−1} and 185 K km s^{−1}, respectively. The resultant FWHM maps of cm-RRL (18–57 km s^{−1}) and mm-RRL (20–44 km s^{−1}) lines are illustrated in Figures 4(a)–(b).

The total RRL linewidth ($\Delta\nu$) is determined mainly by the three contributions, thermal broadening ($\Delta\nu_{\text{the}}$) due to microscopic gas motions, dynamical broadening ($\Delta\nu_{\text{dyn}}$) due to macroscopic gas motions and turbulence, and pressure broadening from collisions with ions and electrons ($\Delta\nu_p$; Galván-Madrid et al. 2012) as

$$\Delta\nu \approx 0.534\Delta\nu_p + (\Delta\nu_{\text{dyn}}^2 + \Delta\nu_{\text{the}}^2 + 0.217\Delta\nu_p^2)^{1/2}. \quad (1)$$

For a pure-hydrogen gas with a given electron temperature T_e , which we assume to be 7030 ± 50 K (Quireza et al. 2006), the thermal broadening is given by

$$\Delta\nu_{\text{the}} = \left(8 \ln 2 k_B \frac{T_e}{m_H} \right)^{1/2} = 17.94 \pm 0.03 (\text{km s}^{-1}), \quad (2)$$

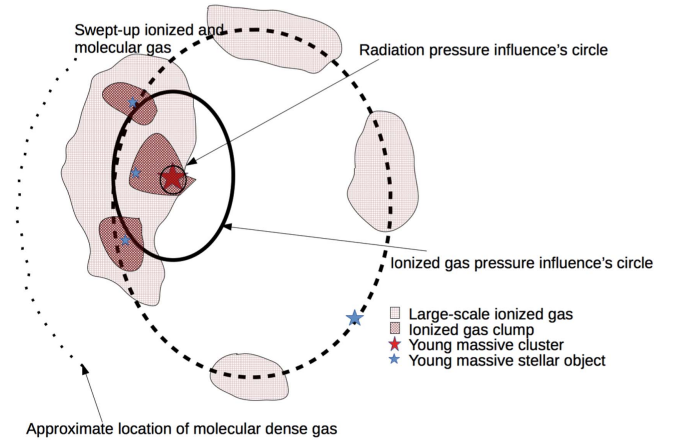


Figure 5. Schematic diagram of ionized gas configuration in the vicinity of the W43-YMC. The segmented line depicts the ionized gas shell under the influence of gas dynamics, the solid line depicts the area under influence of collisions with ions, and the small circle around the YMC depicts the area of radiation pressure influence.

where k_B is the Boltzmann constant and m_H is the hydrogen mass.

Rearranging Equation (4.8) of Brocklehurst & Seaton (1972), the pressure broadening can be roughly estimated as

$$\Delta\nu_p = 4.287 \left(\frac{N}{100} \right)^{7.4} \left(\frac{10^4}{T_e} \right)^{0.1} \left(\frac{n_e}{10^4} \right) (\text{km s}^{-1}), \quad (3)$$

where N is the RRL principal quantum number and n_e is the electron density. For cm-RRL with $N > 151$, $\Delta\nu_p > 15$ km s^{−1}, and the pressure broadening becomes dominant. However, for mm-RRL with $N = 41$ or $N = 42$, $\Delta\nu_p$ is approximately 10^{-3} km s^{−1}, thus mm-RRLs are mainly thermally and dynamically broadened. Therefore, the spatially resolved $\Delta\nu_{\text{dyn}}$ can be estimated from the $\Delta\nu_{\text{mm-RRL}}$ as

$$\Delta\nu_{\text{mm-RRL}}^2 = \Delta\nu_{\text{dyn}}^2 + \Delta\nu_{\text{the}}^2. \quad (4)$$

Conversely, we re-arrange Equation (1) and solve for $\Delta\nu_p$ as

$$\Delta\nu_p = 7.8\Delta\nu_{\text{cm-RRL}} - \sqrt{46\Delta\nu_{\text{cm-RRL}}^2 + 15\Delta\nu_{\text{mm-RRL}}^2}. \quad (5)$$

The resultant pixel-by-pixel maps of the dynamical and pressure broadening of the ionized gas around W43-YMC are plotted in Figures 4(c)–(d) together with the mm-RRL and cm-RRL linewidth maps in Figures 4(a)–(b).

The spatial distributions of these two types of broadening are almost anti-correlated in two-dimensional space. The pressure broadening (4–55 km s^{−1}) dominates inside the shell near the YMC and follows the cm-RRL linewidth distribution while the dynamical broadening (8–36 km s^{−1}) dominates in the shell's edges and follows the mm-RRL linewidth distribution. This trend is in agreement with the expectation from outflowing ionized gas accelerated and produced by a pressure gradient due to expansion, such as in the case of champagne flow model (Tenorio-Tagle 1979; Kim & Koo 2001).

Following Keto et al. (2008), we calculate the electron density n_e as

$$\frac{n_e}{10^5 \text{ cm}^{-3}} = \frac{1}{1.2} \frac{\Delta\nu_p}{\Delta\nu_{\text{the}}} \left(\frac{N}{92} \right)^{-7}. \quad (6)$$

We obtain an electron density of $n_e = 70\text{--}1500\text{ cm}^{-3}$ for W43-Main, which lies within the expected range for giant H II regions (Quireza et al. 2006). The electron density is high, approximately $>1000\text{ cm}^{-3}$, near the location of the YMC.

Dynamical broadening is dominant at about 1 or 2 pc in projected distance above the YMC and resembles the hot gas distribution as seen in the *Herschel* temperature map (Figure 1 (d); see also Nguyen-Luong et al. 2013 or Lin et al. 2016), which suggests that ionized gas pressure contributes to the mixing up of ionized gas with hot dust and neutral gas around this part of the shell. Further evidence for the swept-up activity is the existence of the ionized gas clumps, IC1 to IC3 located at a distance of 2 pc from the YMC, which are also low-density molecular clouds. In the context of an H II region surrounding a YMC, another source that could alter the dynamics of the ionized gas indirectly is the radiation pressure (Krumholz & Matzner 2009). However, it is only important in the inner part of the giant H II region driven by YMCs. The characteristic radius at which gas pressure and radiation pressure (Krumholz & Matzner 2009) are equal is

$$r_{\text{ch}} = 0.023S_{49} \text{ (pc)}, \quad (7)$$

where S_{49} , in units of 10^{49} s^{-1} , is the ionizing luminosity of the ionizing source and $S_{49} = 1$ is the Lyman α ($\text{Ly}\alpha$) ionizing flux of an average OB star. In the case in which the continuum emission is optically thin, we can estimate the ($\text{Ly}\alpha$) ionizing photon flux $N_{\text{Ly}\alpha}$, as described by Mezger & Henderson (1967) as

$$\frac{N_{\text{Ly}\alpha}}{8.9 \times 10^{46}\text{ s}^{-1}} = \frac{S_\nu}{\text{Jy}} \left(\frac{\nu}{\text{GHz}} \right)^{0.1} \left(\frac{T_e}{10^4\text{ K}} \right)^{-0.45} \left(\frac{d}{\text{kpc}} \right)^2, \quad (8)$$

where $\nu = 1.436\text{ GHz}$ is the frequency of the radio continuum observations, $T_e = 7030\text{ K}$ is the electron temperature, and $d = 5.5\text{ kpc}$ is the distance to W43-Main. We estimate the approximated continuum optical depth τ_{cont} from the relation $T_{\text{cont}} = T_e(1 - e^{-\tau_{\text{cont}}})$ for $T_{\text{cont}} \sim 200\text{--}2900\text{ K}$ and $T_e = 7030\text{ K}$. The obtained range of $\tau_{\text{cont}} = 0.025$ to $\tau_{\text{cont}} = 0.44$ shows that the radio continuum at 1.426 GHz is indeed optically thin. Thus, the radio continuum integrated intensity $S_\nu = 55.55 \pm 0.22\text{ Jy}$ of the W43-Main ionized gas shell from THOR (Bihl et al. 2016) gives a $N_{\text{Ly}\alpha}$ of $1.5 \times 10^{50}\text{ s}^{-1}$. The characteristic radius at which the gas pressure and the radiation pressure are equal is $\sim 0.4\text{ pc}$.

In summary, the configuration of ionized gas in W43-YMC can be seen in Figure 5, where radiation pressure is dominated inside the radius of 0.4 pc from the cluster, and ionized gas pressure is dominated at a radius of 0.4 to 2 pc. At a distance of 2 pc from the cluster, the mixing and interaction between ionized gas and pre-existing molecular gas can be found.

We thank the referee and Steve Mairs for constructive comments that improved the quality of the paper. L.B. acknowledges support from CONICYT grant PFB-06. H.B. acknowledges support from the European Research Council

under the Horizon 2020 Framework Program via the ERC Consolidator Grant CSF-648505.

References

- Anderson, L. D., Hough, L. A., Wenger, T. V., Bania, T. M., & Balsaer, D. S. 2015, *ApJ*, **810**, 42
- Bally, J., Anderson, L. D., Battersby, C., et al. 2010, *A&A*, **518**, L90
- Balsaer, D. S., Goss, W. M., & De Pree, C. G. 2001, *AJ*, **121**, 371
- Beuther, H., Bihl, S., Rugel, M., et al. 2016, *A&A*, **595**, A32
- Beuther, H., Meidt, S., Schinnerer, E., Paladino, R., & Leroy, A. 2017, *A&A*, **597**, A85
- Beuther, H., Tackenberg, J., Linz, H., et al. 2012, *A&A*, **538**, A11
- Bihl, S., Beuther, H., Ott, J., et al. 2015, *A&A*, **580**, A112
- Bihl, S., Johnston, K. G., Beuther, H., et al. 2016, *A&A*, **588**, A97
- Blum, R. D., Damineli, A., & Conti, P. S. 1999, *AJ*, **117**, 1392
- Bodenheimer, P., Tenorio-Tagle, G., & Yorke, H. W. 1979, *ApJ*, **233**, 85
- Brocklehurst, M., & Seaton, M. J. 1972, *MNRAS*, **157**, 179
- Carlhoff, P., Nguyen Luong, Q., Schilke, P., et al. 2013, *A&A*, **560**, A24
- Churchwell, E. 2002, *ARA&A*, **40**, 27
- Churchwell, E., Sievers, A., & Thum, C. 2010, *A&A*, **513**, A9
- Contreras, Y., Rathborne, J. M., Guzman, A., et al. 2017, *MNRAS*, **466**, 340
- Csengeri, T., Bontemps, S., Wyrowski, F., et al. 2017, *A&A*, **601**, A60
- Dale, J. E., & Bonnell, I. 2011, *MNRAS*, **414**, 321
- Fujii, M. S. 2015, *PASJ*, **67**, 59
- Galván-Madrid, R., Goddi, C., & Rodríguez, L. F. 2012, *A&A*, **547**, L3
- Gordon, M. A., & Walmsley, C. M. 1990, *ApJ*, **365**, 606
- Guzmán, A. E., Garay, G., Rodríguez, L. F., et al. 2014, *ApJ*, **796**, 117
- Hill, T., Motte, F., Didelon, P., et al. 2011, *A&A*, **533**, A94
- Jones, P. A., Burton, M. G., Cunningham, M. R., et al. 2012, *MNRAS*, **419**, 2961
- Keto, E., Zhang, Q., & Kurtz, S. 2008, *ApJ*, **672**, 423
- Kim, K.-T., & Koo, B.-C. 2001, *ApJ*, **549**, 979
- Kim, W.-J., Wyrowski, F., Urquhart, J. S., Menten, K. M., & Csengeri, T. 2017, *A&A*, **602**, A37
- Krumholz, M. R., & Matzner, C. D. 2009, *ApJ*, **703**, 1352
- Lester, D. F., Dinerstein, H. L., Werner, M. W., et al. 1985, *ApJ*, **296**, 565
- Lin, Y., Liu, H. B., Li, D., et al. 2016, *ApJ*, **828**, 32
- Louvet, F., Motte, F., Gusdorf, A., et al. 2016, *A&A*, **595**, A122
- Louvet, F., Motte, F., Hennebelle, P., et al. 2014, *A&A*, **570**, A15
- Mezger, P. G., & Henderson, A. P. 1967, *ApJ*, **147**, 471
- Motte, F., Nguyễn Luong, Q., Schneider, N., et al. 2014, *A&A*, **571**, A32
- Motte, F., Schilke, P., & Lis, D. C. 2003, *ApJ*, **582**, 277
- Natta, A., Walmsley, C. M., & Tielens, A. G. G. M. 1994, *ApJ*, **428**, 209
- Nguyen-Luong, Q., Motte, F., Carlhoff, P., et al. 2013, *ApJ*, **775**, 88
- Nguyen-Luong, Q., Motte, F., Schuller, F., et al. 2011, *A&A*, **529**, A41
- Nguyen-Luong, Q., Nguyen, H. V. V., Motte, F., et al. 2016, *ApJ*, **833**, 23
- Peters, T., Longmore, S. N., & Dullemond, C. P. 2012, *MNRAS*, **425**, 2352
- Portegies Zwart, S. F., McMillan, S. L. W., & Gieles, M. 2010, *ARA&A*, **48**, 431
- Purcell, C. R., Hoare, M. G., Cotton, W. D., et al. 2013, *ApJS*, **205**, 1
- Quireza, C., Rood, R. T., Bania, T. M., Balsaer, D. S., & Maciel, W. J. 2006, *ApJ*, **653**, 1226
- Rahman, M., Matzner, C. D., & Moon, D.-S. 2013, *ApJ*, **766**, 135
- Saral, G., Hora, J. L., Audard, M., et al. 2017, *ApJ*, **839**, 108
- Schneider, N., Csengeri, T., Hennemann, M., et al. 2012, *A&A*, **540**, L11
- Sewilo, M., Churchwell, E., Kurtz, S., Goss, W. M., & Hofner, P. 2011, *ApJS*, **194**, 44
- Smirnov, G. T., Sorochenko, R. L., & Walmsley, C. M. 1995, *A&A*, **300**, 923
- Tan, J. C., Beltrán, M. T., Caselli, P., et al. 2014, in *Protostars and Planets VI*, ed. H. Beuther et al. (Tucson, AZ: Univ. Arizona Press), 149
- Tenorio-Tagle, G. 1979, *A&A*, **71**, 59
- Walmsley, C. M. 1990, *A&AS*, **82**, 201
- Walmsley, C. M., Churchwell, E., & Terzian, Y. 1981, *A&A*, **96**, 278
- Zhang, B., Moscadelli, L., Sato, M., et al. 2014, *ApJ*, **781**, 89